MNRAS **000**, 1–12 (2019) Preprint 4 November 2019 Compiled using MNRAS LaTeX style file v3.0

Internal Gravity Wave Breaking in White Dwarf Binaries

Yubo Su,[1], Daniel Lecoanet,[2] Dong Lai,[1]
[1] *Cornell Center for Astrophysics and Planetary Science, Department of Astronomy, Cornell University, Ithaca, NY 14853, USA*
[2] *Princeton Center for Theoretical Science, Princeton University, Princeton, NJ 08544, USA*

Accepted XXX. Received YYY; in original form ZZZ

ABSTRACT
In sufficiently compact white dwarf binaries, dynamical tides raise a train of internal gravity waves that propagate towards the surface. We perform 2D numerical simulations of these waves undergoing nonlinear wave breaking in an incompressible, isothermal atmosphere. After an initial transient phase, we find that these waves induce a sharp transition between a non-rotating core and synchronously rotating envelope. We find evidence that the width of this transition layer is bound from below by the Kelvin-Helmholtz Instability. We provide analytical formulae for absorption and reflection of incident waves off the critical layer up to prefactors of order unity. These prefactors converge to constant values when artificial dissipation is decreased. We provide dimensionless criteria necessary to resolving momentum transfer within the critical layer. Finally, we speculate on the application of our model to tidal synchronization and heating in astrophysical systems.

Key words: white dwarfs – hydrodynamics – binaries:close – waves

1 INTRODUCTION

[Below copied from proposal, will rewrite]

Compact white dwarf (WD) binary systems, with orbital periods in the range of minutes to hours, are important for a range of astrophysical problems. They are the most important sources of gravitational waves (GWs) for the Laser Interferometric Space Antenna (LISA) (Nelemans 2009). They are also thought to produce interesting optical transients such as underluminous supernovae (Perets et al. 2010), Ca-rich fast transients (García-Berro et al. 2017), and tidal novae (Fuller & Lai 2012b). Most importantly, they have been proposed as the likely progenitors of type Ia supernovae (e.g. Iben Jr & Tutukov 1984; Webbink 1984 or more recently Gilfanov & Bogdán 2010; Maoz et al. 2010). While presently only a few tens of compact WD binaries are known (Korol et al. 2017), *Gaia* (currently gathering data) is expected to expand the catalog to a few hundreds (Korol et al. 2017) (results based on *Gaia*'s second data release have already begun to appear Shen et al. 2018; Kilic et al. 2018), and the Large Synoptic Survey Telescope (LSST, first light scheduled for 2020) will likely detect a few thousand more (Korol et al. 2017). These observations will significantly advance the understanding of WD binaries and their evolution.

In spite of the broad importance of WD binaries, the evolution of these systems prior to their final mergers is not well understood. Much of this uncertainty comes from our imprecise understanding of tidal interactions, which play an important role during a compact WD binary's inspiral (Fuller & Lai 2012a). Previous studies have shown that these interactions manifest as tidal excitation of internal gravity waves (IGW), waves in the WD fluid restored by the buoyancy force due to density stratification (Fuller & Lai 2011). As these waves propagate outwards towards the WD surface, they grow in amplitude until they break, as do ocean waves on a shore, and transfer both energy and angular momentum from the binary orbit to the outer envelope of the WD (Fuller & Lai 2011, 2012a).

Previous works have found that the dissipation of IGW can generate significantly more energy than thermal radiation from the isolated WD surface and is thus a major contributor to the WD energy budget (Fuller & Lai 2012a, 2013). However, these works parameterized the wave breaking process in an ad hoc manner. The details of dissipation, namely the location and spatial extent of the wave breaking, affect the observable outcome: dissipation near the surface of the WD can be efficiently radiated away and simply brightens the WD, while dissipation deep in the WD envelope causes an energy buildup that results in energetic flares (Fuller & Lai 2012b). Works in other fields based on numerical simulations show that strongly nonlinear wave breaking behaves differently than predictions based in linear and weakly nonlinear theory (Winters & D'Asaro 1994; Barker & Ogilvie 2010). Such fully nonlinear numerical simulations have not been performed for WDs.

In Section 2, we will describe the system of equations we will use to analyze IGW breaking. In Section 3, we discuss relevant analytical results. In Section 5 we present the results of numerical simulations. Finally, in Section 6 we discuss the results of the preceeding section.

2 PROBLEM DESCRIPTION

We consider a incompressible, isothermal fluid, representative of degenerate matter in WDs. We use barotropic equation of state $P(\rho, T) = P(\rho)$ as a first approximation. As we are interested in dynamics far from the center of the WD, we approximate the gravitational field as uniform. We model the background density stratification as $\overline{\rho} = \overline{\rho}_0 e^{-z/H}$ for some reference density $\overline{\rho}_0$ (we generally notate background quantities with overbars and perturbation quantities with primes). Finally, we consider a 2D fluid for computational feasibility: while it is well-known wave breaking is a 3D process (Klostermeyer 1991; Winters & D'Asaro 1994), the dynamical effect of the breaking process is likely to be similar in 2D (Barker & Ogilvie 2010).

The Euler equations for an incompressible, barotropic fluid in a uniform gravitational field are

$$\nabla \cdot \mathbf{u} = 0, \tag{1a}$$

$$\frac{\mathrm{D}\rho}{\mathrm{D}t} = 0, \tag{1b}$$

$$\frac{\mathrm{D}\mathbf{u}}{\mathrm{D}t} + \frac{\nabla P}{\rho} + g\hat{\mathbf{z}} = 0. \tag{1c}$$

$\frac{\mathrm{D}}{\mathrm{D}t} = \frac{\partial}{\partial t} + (\mathbf{u} \cdot \nabla)$ is the Lagrangian or material derivative, and $\mathbf{u}, \rho, P$ denote the velocity field, density and pressure respectively. We denote $-g\hat{\mathbf{z}}$ constant gravitational acceleration. Note that at hydrostatic equilibrium $\frac{\partial}{\partial t} = 0$ we have $\nabla\overline{P} = -\overline{\rho}g\hat{\mathbf{z}}$ and so $\overline{P} = \overline{\rho}gH$. A vertically-stratified shear flow $\overline{u}_x(z)\hat{\mathbf{x}}$ is permitted at hydrostatic equilibrium, but we will assume no background flow, so $\mathbf{u} = \mathbf{u}'$. Physically, this assumption corresponds to a non-rotating star, or going to the corotating frame of a rigidly rotating star.

In practice, it is convenient to introduce the coordinate $\Upsilon = \ln\frac{\rho}{\overline{\rho}}$ (e.g. Lecoanet et al. 2014). This both identically enforces $\rho > 0$ and eliminates the stiff term $\frac{\nabla P}{\rho}$. We also define reduced pressure $\varpi = \frac{P}{\rho}$. Then, we may rewrite the second two equations of Equation 1 as

$$\frac{\mathrm{D}\Upsilon}{\mathrm{D}t} + u_z\frac{\partial \ln\overline{\rho}}{\partial z} = 0, \tag{2a}$$

$$\frac{\mathrm{D}\mathbf{u}}{\mathrm{D}t} + \nabla\varpi + \varpi\nabla\Upsilon - \frac{\varpi}{H}\hat{\mathbf{z}} + g\hat{\mathbf{z}} = 0. \tag{2b}$$

In the new coordinates, hydrostatic equilibrium corresponds to $\Upsilon = 0, \overline{\varpi} = gH$.

3 INTERNAL GRAVITY WAVES: THEORY

3.1 Linear Analysis

In the small perturbation limit, where flow velocities are small compared to the characteristic space and time scales $\frac{\partial}{\partial t} \gg \mathbf{u}' \cdot \nabla$, we may linearize Equation 2. The solution in this linear regime is given by (Drazin 1977; Dosser & Sutherland 2011b):

$$u_z'(x, z, t) = Ae^{z/2H}\cos\left(k_x x + k_z z - \omega t\right), \tag{3}$$

where A is the amplitude and ω satisfies dispersion relation

$$\omega^2 = \frac{N^2 k_x^2}{k_x^2 + k_z^2 + \frac{1}{4H^2}}. \tag{4}$$

Our equations are valid in the limit of large sound speed $c_s \to \infty$, in which the *Brunt-Väisälä frequency*

$$N^2 \equiv g^2\left(\frac{\mathrm{d}\rho}{\mathrm{d}P} - \frac{1}{c_s^2}\right) = \frac{g}{H}, \tag{5}$$

is constant. Other dynamical quantities are simply related to u_z' (see e.g. Dosser & Sutherland 2011b).

In the short-wavelength/WKB limit $|k_z H| \gg 1$, the solution exhibits the following characteristics:

- The amplitude of the wave grows with z as $e^{z/2H}$. Thus, the linear approximation is always violated for sufficiently large z.
- The phase and group velocities are respectively:

$$\mathbf{c}_p = (k_x\hat{\mathbf{x}} + k_z\hat{\mathbf{z}})\frac{\omega}{k_x^2 + k_z^2 + \frac{1}{4H^2}}, \tag{6}$$

$$\mathbf{c}_g = N\frac{\left(k_z^2 + \frac{1}{4H^2}\right)\hat{\mathbf{x}} - (k_x k_z\hat{\mathbf{z}})}{\left(k_x^2 + k_z^2 + \frac{1}{4H^2}\right)^{3/2}}. \tag{7}$$

We note $\mathbf{c}_p \cdot \mathbf{c}_g = \mathcal{O}\left((k_z H)^{-2}\right) \approx 0$. In the Boussinesq approximation where density stratification outside of N^2 is completely neglected, the phase and group velocity are exactly orthogonal (Drazin 1977; Dosser & Sutherland 2011a). We use the convention where upward propagating IGW have $c_{g,z} > 0$, $k_z < 0, k_x > 0$.

- The averaged horizontal momentum flux F is

$$F \equiv \left\langle \rho u_x' u_z' \right\rangle_x \equiv \frac{1}{L_x}\int_0^{L_x} \rho u_x' u_z' \,\mathrm{d}x, \tag{8}$$

$$\approx -\frac{A^2}{2}\overline{\rho}_0\frac{k_z}{k_x}, \tag{9}$$

Thus, indeed $F > 0$ for an upward propagating IGW $c_{g,z} > 0$.

3.2 Wave Generation

To model continuous excitation of IGWs deep in the WD interior propagating towards the surface, we use a volumetric forcing term to excite IGW near the bottom of the simulation domain. Our forcing excites both IGWs propagating upwards, imitating a wave tidally excited deeper in the WD, and downwards, which are damped away by the damping layers described in subsection 4.2.

As not to interfere with the incompressibility constraint, we force the system on the density equation. We implement forcing with strength C localized around z_0 with small width σ by replacing Equation 2a with

$$\frac{\mathrm{D}\Upsilon}{\mathrm{D}t} + u_z'\frac{\partial \ln\overline{\rho}}{\partial z} = Ce^{-\frac{(z-z_0)^2}{2\sigma^2}}\cos\left(k_x x - \omega t\right). \tag{10}$$

Using a narrow Gaussian profile excites a broad z power spectrum, but only the k_z satisfying dispersion relation Equation 4 for the given $k_x, \omega(k_x, k_z)$ will propagate.

In the linearized system, the effect of this forcing can be solved exactly. If we approximate $k_z H \gg 1, \sigma \ll H$, the solution can be approximated as two plane waves propagating away from the forcing zone

$$u_z'(x, z, t) \approx \frac{C}{2k_z}\frac{gk_x^2}{\omega^2}e^{-\frac{k_z^2\sigma^2}{2}}\sqrt{2\pi\sigma^2}\times \begin{cases} e^{\frac{z-z_0}{2H}}\sin\left(k_x x + k_z(z - z_0) - \omega t + \frac{k_z\sigma^2}{2H}\right) & z > z_0 \\ e^{\frac{z-z_0}{2H}}\sin\left(k_x x - k_z(z - z_0) - \omega t + \frac{k_z\sigma^2}{2H}\right) & z < z_0 \end{cases}. \tag{11}$$

The $z > z_0$ region models an upward propagating IGW wavetrain excited deep in the atmosphere. A derivation of this result is provided in Section A.

3.3 Wave Breaking Height

Above, we neglected advective terms $\frac{\partial}{\partial t} \gg \mathbf{u}' \cdot \nabla$. However, since $|\mathbf{u}'| \propto e^{z/2H}$ in an infinite domain all IGWs eventually grow to nonlinear amplitudes and break. Nonlinear wave breaking is expected to be important in WDs (Fuller & Lai 2011, 2012a). We can estimate the height of wave breaking using $\frac{|\mathbf{u}'||\mathbf{k}|}{\omega} \sim 1$. This can be rewritten using the Lagrangian displacement $-i\omega\xi' = \mathbf{u}'$:

$$\xi_z k_z \gtrsim 1. \tag{12}$$

An equivalent estimate given by (Andrews & Mcintyre 1976; Dosser & Sutherland 2011b) is that IGWs break when the wave-induced mean flow is equal to the horizontal phase velocity

$$\overline{U}(z) = \frac{\langle u_x u_z \rangle_x}{c_{g,z}} \sim \frac{\omega}{k_x}, \tag{13}$$

where $\bar{U}(z) \equiv \langle u_x \rangle_x$ is the mean flow of the fluid. Equation 13 provides a leading-order estimate for $\bar{U}(z)$ which may further evolve over time (see subsection 3.4); for a general mean flow, Equation 13 also defines the criterion for a *critical layer*. This wave-induced mean flow is analogous to Stokes' drift for surface waves and can be derived by considering the propagation of F (Equation 8) into a medium at rest. Evaluating Equation 13 yields agreement with Equation 12.

3.4 Critical Layer Dynamics

The detailed onset of wave breaking has been laid out in a few key papers (Drazin 1977; Klostermeyer 1991; Winters & D'Asaro 1994), where instabilities transfer momentum out of the IGW through daughter modes into the mean flow of the fluid. When viscosity is sufficiently weak (see subsection 6.1 for a discussion of this assumption in WDs), a non-uniform shear flow and eventually a critical layer develop. The further evolution of the critical layer with the incident IGW is thought to be responsible for tidal synchronization in stellar binaries (Zahn 1975; Goldreich & Nicholson 1989) as well as terrestrial phenomena such as the quasi-biennial oscillation (Lindzen & Holton 1968).

The behavior of an IGW incident upon a critical layer was first studied in the inviscid, linear regime in (Booker & Bretherton 1967), which found nearly complete absorption of the IGW. In particular, the incident wave has amplitude reflection and transmission coefficients that can be expressed in terms of the local Richardson number Ri at the height of the critical layer z_c:

$$\mathrm{Ri} \equiv \left.\frac{N^2}{\left(\frac{\partial \overline{U}}{\partial z}\right)^2}\right|_{z_c}, \tag{14}$$

$$\mathcal{R}_A = e^{-2\pi\sqrt{\mathrm{Ri}-\frac{1}{4}}}, \qquad \mathcal{T}_A = e^{-\pi\sqrt{\mathrm{Ri}-\frac{1}{4}}}. \tag{15}$$

In the $\mathrm{Ri} \gg 1$ limit, $\mathcal{R}, \mathcal{T} \ll 1$ and the incident wave is completely absorbed to a good approximation.

This result extends to viscous fluids (Hazel 1967), but weakly nonlinear theory (Brown & Stewartson 1982) and numerical simulations (Winters & D'Asaro 1994) suggest that nonlinear effects may significantly enhance reflection and transmission.

Consider the horizontal momentum transfer at the critical layer. Any incident horizontal momentum flux absorbed by the fluid must manifest as additional horizontal momentum of the shear flow. Since the mean flow cannot exceed $\overline{U}_c \equiv \omega/k_x$, the horizontal phase velocity of the incident wave, the critical layer will instead propagate downward in response to the incident momentum flux. The horizontal momentum of the shear flow satisfies

$$\frac{\partial}{\partial t}\int \overline{\rho}(z)\overline{U}(z,t)\,\mathrm{d}z - \Delta F = 0, \tag{16}$$

where $\Delta F > 0$ is the absorbed horizontal momentum. Assuming $\overline{U}(z > z_c) = \overline{U}_c, \overline{U}(z < z_c) = 0$, this condition becomes

$$\overline{\rho}(z_c)\overline{U}_c \frac{\mathrm{d}z_c}{\mathrm{d}t} = \Delta F. \tag{17}$$

If ΔF is constant in time, $z_c(t)$ has analytical solution

$$z_c(t) = -H \ln \frac{\overline{\rho}(t=0) + t\frac{\Delta F}{\overline{U}_c H}}{\overline{\rho}_0}, \tag{18}$$

where $\overline{\rho}(t_0)$ is the density at the critical layer height at $t = 0$.

4 INTERNAL GRAVITY WAVES: WEAKLY FORCED NUMERICAL SIMULATIONS

4.1 Numerical Setup

We verify the analytic theory of Section 3 by running weakly forced direct numerical simulations using the pseudo-spectral code Dedalus (Burns et al. 2016; Burns et al. 2019). IGWs are excited deep within WDs and must propagate across many density scale heights before reaching the surface. The waves stay linear until they are within a few scale heights of the breaking height. We thus simulate only the upper part of the WD. Although turbulence driven by wave breaking is fundamentally 3D (Klostermeyer 1991), we simplify the problem by restricting our simulations to two dimensions. Future work will study the problem in 3D spherical geometry.

For numerical convenience, we simulate equations Equation 1a, Equation 2b, and Equation 10 in a Cartesian box with size L_x, L_z. The x direction represents the azimuthal direction in a star, and the z direction represents the radial direction. We thus choose periodic boundary conditions in the x direction. We also use periodic boundary conditions in the z direction, but we damp perturbations to zero near the top/bottom of the domain to capture their distinct behavior (described in subsection 4.2). We expand all variables as a Fourier series with N_x and N_z modes, and use the 3/2 dealiasing rule to avoid aliasing errors in the nonlinear terms (Boyd 2001).

The geometry of our simulation domain is fixed by one further parameter: z_0 the forcing location. We choose $L_z = 10H$ to give $\sim e^3$ amplitude growth between the damping zones. We force at $z_0 = 2H = 0.2L_z$ within width $\sigma = 0.078H$, sufficiently far from the lower damping zone and permit sufficient room for the upward moving wave to grow as $\propto e^{z/2H}$. Finally, we want similar grid spacing $\frac{L_x}{N_x} \sim \frac{L_z}{N_z}$, guided by the intuition that turbulence is approximately isotropic, so we use $L_x = 4H$ and $N_z/N_x = 4$.

The time integration uses a split implicit-explicit third-order scheme where certain terms are treated implicitly and the remaining terms are treated explicitly. A third-order, four-stage DIRK-ERK scheme (Ascher et al. 1997) is used with adaptive timesteps computed from advective Courant-Friedrichs-Lewy (CFL) time. Specifically, we use $\Delta t = 0.7\min(\Delta x/u_x, \Delta z/u_z)$, where the minimum is taken over every grid point in the domain and $\Delta x, \Delta z$ are the grid spacings in the x and z directions respectively.

We non-dimensionalize the problem such that $H = N = \rho_0 = 1$. The physics of the simulation is then fixed by the four remaining parameters k_x, ω, C, ν. We describe our choices for these parameters below:

- k_x: Tidally excited waves in stars generally have $\ell = 2$, corresponding to a very small $k_\perp \sim 1/R$, where R is the radius of the star. We use the smallest wavenumber in our simulation, $k_x = 2\pi/L_x$.

- ω: We choose ω by evaluating the dispersion relation $\omega(k_x, k_z)$ for a desired k_z. We pick $|k_z H| = 2\pi$ to ensure the waves are very well resolved in all of our simulations. Note however that tidally forced IGWs typically have $\omega \ll N$, or equivalently $k_r/k_\perp \sim k_r R \gg 1$. This requires $k_z H \gtrsim 1$, which is only marginally satisfied in our simulations.
- C: In our linear simulations, we first choose C forcing strength such that $\xi_z k_z \ll 1$ is satisfied everywhere in the simulation domain. This constrains C by Equation 11.
- ν: Nonlinear effects transfer wave energy from the injection wavenumber $\mathbf{k}$ to larger wavenumbers. Our spectral method does not have any numerical viscosity, so diffusivity must be introduced into the equations to regularize the systems. We add viscosity and diffusivity to the system in a way that conserves horizontal momentum (see Appendix B for details). When the forcing is weak, we may set $\nu = 0$ because there is negligible energy transfer between modes.

Finally, we use initial conditions $\mathbf{u}(x,z,0) = \Upsilon(x,z,0) = 0, \varpi(x,z,0) = 1$ corresponding to hydrostatic equilibrium and no initial fluid motion.

4.2 Damping Layers

We aim to damp waves that reach the edge of the simulation domain without inducing nonphysical reflection. To do so, we replace material derivatives in Equation 2 with:

$$\frac{\mathrm{D}}{\mathrm{D}t} \to \frac{\mathrm{D}}{\mathrm{D}t} + \Gamma(z)\Upsilon,$$
$$\Gamma(z) = \frac{1}{2\tau}\left[2 + \tanh\frac{z - z_T}{\Delta z} + \tanh\frac{z_B - z}{\Delta z}\right], \tag{19}$$

where $z_B = 0.05L_z, z_T = 0.95L_z$ are the boundaries of the damping zone. This strongly damps perturbations below z_B and above z_T with damping time τ, negligibly affects dynamics between z_B, z_T and has transition width governed by Δz. We use $\Delta z = 0.025L_z$ and $\tau = 1/15N$. This prescription is similar to (Lecoanet et al. 2016) and has the advantage of being smooth, important for spectral methods. Further details of our implementation of the fluid equations in Dedalus are described in Appendix B.

4.3 Simulation Results

We describe the results of a simulation with $C = 1.64 \times 10^{-7}$ such that $\xi_z k_z \ll 1$ everywhere. In particular, $\xi_z k_z \approx 5 \times 10^{-5}$ just above the forcing zone.

We expect the waves to follow the solution given by Equation 11. Along with incompressibility (Equation 1a), we obtain a complete analytical solution for flow velocities $\mathbf{u}_{al}(x,z,t)$. The amplitude of the observed IGW in the simulation field $\mathbf{u}$ relative to analytical solution $\mathbf{u}_{al}$ over some region $z \in [z_b, z_t]$ can be estimated with estimator $\hat{A}_i(t)$ (subscript i denotes incident wave)

$$\hat{A}_i(t) = \frac{\int\limits_{z_b}^{z_t}\int\limits_0^{L_x} \overline{\rho}\,(\mathbf{u}\cdot\mathbf{u}_{al})\;\mathrm{d}x\mathrm{d}z}{\int\limits_{z_b}^{z_t}\int\limits_0^{L_x} \overline{\rho}\,|\mathbf{u}_{al}|^2\;\mathrm{d}x\mathrm{d}z} \tag{20}$$

If $\mathbf{u} = \mathbf{u}_{al}$, then $\hat{A}_i(t) = 1$. The energy norm is a traditional normalization choice such that the overlap between $\mathbf{u}, \mathbf{u}_{al} \propto e^{z/2H}$ is evenly weighted throughout the integration region.

For a simulation satisfying $\xi_z k_z \ll 1$ everywhere, we expect $\hat{A}_i(t) = 1$ when integrated between the forcing and damping zones, i.e. $z_b \gtrsim z_0, z_t \lesssim z_T$ (z_0, z_T are defined in Equation 10 and Equation 19 respectively). For consistency with the nonlinear case later, we choose $z_b = z_0 + 3\sigma, z_t = z_b + H$ (using $z_t = z_T - \Delta z$ just below the damping layer instead does not change the results). The resulting measurement of $\hat{A}_i(t)$ is shown in Figure 1.

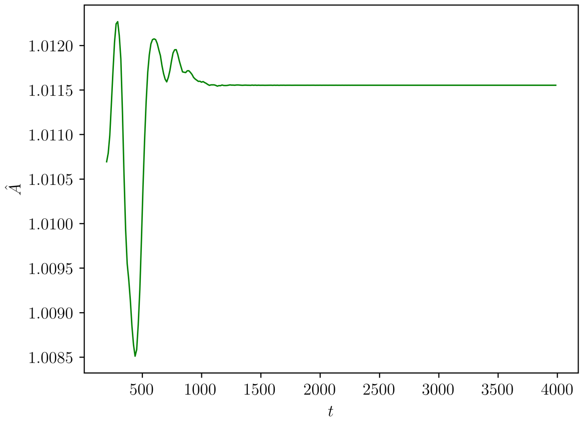

Figure 1. Amplitude of excited wave over time in weak forcing simulation, computed using Equation 20. $\hat{A}_i(t) = 1$ corresponds to perfect agreement with the analytical estimate. After an initial transient phase, we observe great agreement with Equation 11, and in particular $\hat{A}_i(t)$ asymptotes to ≈ 1, implying continuous excitation of identical IGW with the expected amplitude.

The analytical theory also predicts that the horizontal momentmum flux $F(z,t)$ should be independent of z between the forcing zone where it is generated and the damping zone where it is dissipated (Equation 8). We make may a slightly more accurate estimate of the flux carried in the IGW by directly substituting $\mathbf{u}_{al}$ into Equation 8. Calling this estimate

$$F'_{al}(z) \equiv \left\langle \overline{\rho} u_{al,x} u_{al,z} \right\rangle_x \tag{21}$$

we may then measure the agreement of our simulation with analytical expectation by computing

$$\hat{F}(z,t) \equiv \frac{\langle \rho u_x u_z \rangle_x}{F'_{al}}. \tag{22}$$

Figure 2 shows that $\hat{F}(z) \approx 1$ between z_0 and z_T, as expected.

5 INTERNAL GRAVITY WAVES: NONLINEAR SIMULATION

To perform simulations of wave breaking phenomena, we use the same values as subsection 4.1 except for C and ν. In particular, we choose C such that $\xi_z k_z|_{z_0} = 0.1$ in the forcing zone. The linear solution predicts $\xi_z k_z \sim 4.25$ at the upper damping zone z_T. The dissipation parameter ν was varied across the various simulations. To quantify ν, we define dimensionless Reynolds number

$$\mathrm{Re} \equiv \frac{\omega}{\nu k_z^2}. \tag{23}$$

A table of our simulations can be found in Table 1.

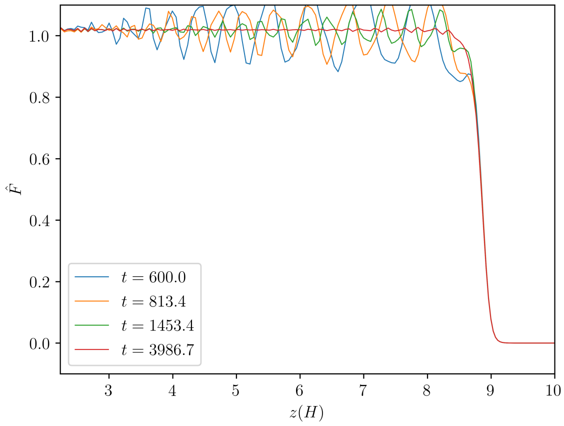

Figure 2. Equation 22 as a function of z at select times t. As initial transients die out, $\hat{F}(z,t) = 1$ to very good agreement above the forcing zone $z > z_0 = 2H$ and below the damping zone $z \lesssim z_T = 9.5H$. The flux excited in the forcing zone is transported without loss to the top of the domain, where it is dissipated by the damping layer (see subsection 4.2) without reflection.

Resolution	Re
1024×4096	2048
768×3072	1024
512×2048	512
256×1024	341
256×1024	205
256×1024	146

Table 1. Table of simulation resolutions.

5.1 Numerical Simulation Results

A full video of our higher-resolution run at $N_x = 768$, $N_z = 3072$, Re = 1024 is available online[1]. We take this to be our fiducial simulation for the remainder of this paper, though other simulations show qualitatively similar behavior.

In Figure 3, we present snapshots of the velocity field $\mathbf{u}$ at various interesting phases of the simulation.

(i) At early times (top left panel), the flow resembles a linear IGW lower in the simulation domain but breaks down into smaller-scale features at higher z. Some characteristic swirling motion can be seen in both u_x, u_z, highly suggestive of Kelvin-Helmholtz instabilities.

(ii) At a slightly later time (top right panel), the mean flow in u_x has become much more prominent and the critical layer z_c has become much more definite. Small-scale fluctuations are still present in u_z but at smaller amplitudes due to being in a denser region of the fluid.

(iii) In the bottom left panel, the critical layer transition is now extremely sharp, and small swirls of limited vertical extent at the location of the critical layer in u_z suggest that the Kelvin-Helmholtz instability is responsible for regulating the minimum width of this transition. This is supported by the conclusions in subsection 5.3.

(iv) The end of the simulation shows very few significant qualitative differences from the previous snapshot, suggesting that the latter half of our simulation is temporally converged.

[1] http://www.princeton.edu/ lecoanet/data/breaking_wave.mov

In Figure 4, we plot $\overline{U}$ and $\hat{F}$ as a function of z at the times depicted in Figure 3. While the behavior of $\overline{U}$ seems to conform qualitatively with the predictions of subsection 3.4, the behavior of $\hat{F}$ exhibits two notable features: (i) the incident flux seems to fluctuate greatly with time, and (ii) there seems to be a small transmitted feature at many of the later times. We will discuss further these features in subsection 5.4, after first analyzing the propagation of the critical layer.

5.2 Propagating Critical Layer

For the simulation shown in Figure 4, we may analyze the location of the critical layer. As the simulations are very noisy, we measure the location of the critical layer using an average of where flux deposition occurs

$$\begin{aligned}
z_{c,\min} &= \operatorname*{argmin}_z \left\{ z : F(z) < 0.3F'_{al} \right\},\\
z_{c,\max} &= \operatorname*{argmax}_z \left\{ z : F(z) > 0.3F'_{al} \right\},\\
z_c &\equiv \frac{z_{c,\min} + z_{c,\max}}{2}.
\end{aligned} \tag{24}$$

This was found to a relatively stable estimator of the critical layer location. Other estimators were used and do not significantly change the results of the analysis.

The evolution of z_c depends on the deposited flux $\Delta F(t)$ per Equation 17. To estimate $\Delta F(t)$ across the critical layer z_c from the data, we defined:

$$F_<(t) = \langle F(z) \rangle_{z \in [z_c - \Delta z - H, z_c - \Delta z]}, \tag{25}$$
$$F_>(t) = \langle \{F(z) : F(z) < 0\} \rangle_{z \in [z_c, z_c + \Delta z]}, , \tag{26}$$
$$\Delta F(t) \equiv F_>(t) - F_<(t). \tag{27}$$

$\langle \dots \rangle_{z \in [z_a, z_b]}$ denotes averaging over interval $[z_a, z_b]$. Below the critical layer, we average over an interval of length $\frac{2\pi}{k_z}$ a full vertical wavelength. The offset Δz is necessary to make a measurement of the incident flux unaffected by the turbulence within the critical layer itself. The height of the critical layer is limited by Ri $\lesssim 1$, which bounds its vertical extent $\sim \frac{1}{k_z}$. We empirically found an offset of $\Delta z = \frac{3}{k_z}$ was necessary to be sufficiently far from strong fluctuations near the critical layer.

Above the critical layer, waves decay over a much smaller vertical extent as they have larger z wavenumbers thanks to the shear flow Doppler shift. Accurate measurement of these fluctuations above the critical layer is important to measuring the transmission feature accurately, seen in Figure 4 to be weak and attenuate quickly.

Finally, we may plot the measured z_c against two semi-analytic predictors: (i) integration of Equation 17 using the measured $\Delta F(t)$, and (ii) substituting the time-averaged $\langle \Delta F \rangle_t$ (over the entire length of the simulation) into Equation 18. Since $z_c(t)$ is both stable and less well-defined at early times (when the critical layer is thick and transient behavior is still strong), we instead integrate backwards from the end of the simulation, using $z_c(t_f)$ as initial condition. The resulting predictors are depicted in Figure 5. The good agreement between the evolution of $z_c(t)$ and its estimate via $\Delta F(t)$ and Equation 17 are noteworthy.

Also of interest is the behavior of the time-averaged $\langle \Delta F \rangle_t = 0.71F'_{al}$ predictor, which serves mostly as a fiducial in the plot. The general agreement clearly demonstrates $\Delta F < F'_{al}$ and that momentum flux absorption is incomplete. However, its underprediction of critical layer velocity at early times contrasts with its overprediction at later times. This suggests that momentum flux absorption changes

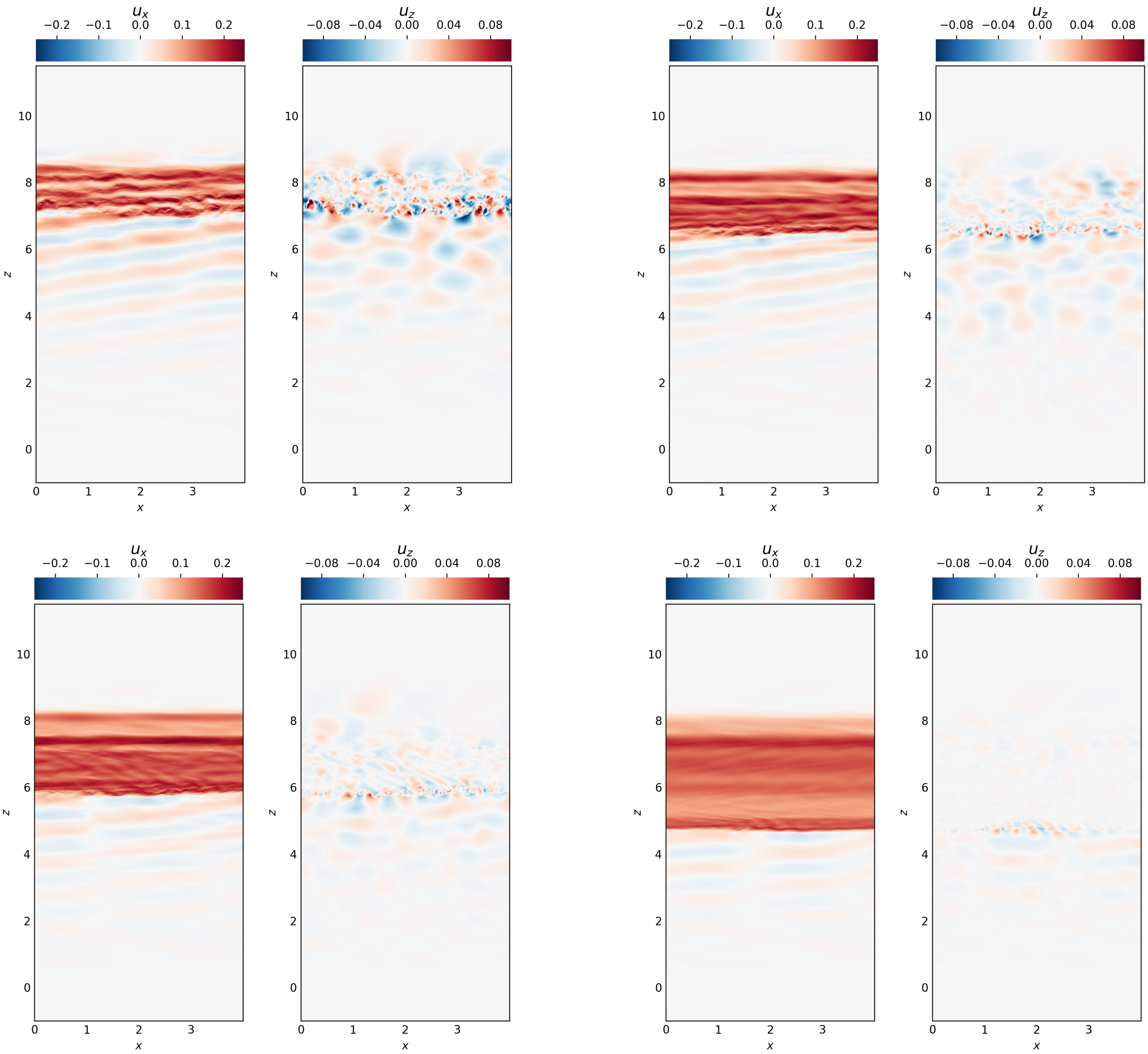

Figure 3. Snapshots of u_x, u_z in the fiducial simulation illustrating distinct phases of the evolution of the flow. Note that $\overline{U}_c \approx 0.16$ for the parameters used. The four times depicted are $t = 413.4$ (top left), $t = 658.5$ (top right), $t = 1171.4$ (bottom left), and $t = 3437.8$ (bottom right). The four snapshots illustrate the initial transient wave breaking phase, formation of a distinct critical layer, steepening of the critical layer, and propagation of the critical layer respectively.

significantly over time, which is in line with the observations in the subsequent subsection 5.4.

5.3 Kelvin-Helmholtz Instability and Critical Layer Width

The observation of reflected/transmitted waves is in accordange with previous studies as discussed in subsection 3.3. Studies have shown that a local Richardson number Ri $\sim 1/4$ corresponds to the onset of reflectivity. This Ri also corresponds to the onset of the Kelvin-Helmholtz instability (KHI). Indeed, in our simulations, visual inspection suggests the KHI is present in the critical layer (see Figure 3). It is natural to suspect then that the shear flow cannot steepen any further than KHI onset. To verify this, we decided to compute a local Ri for the shear flow around the critical layer.

Since fluid instabilities are local, Ri must be measured in the immediate vicinity of a fluid parcel. Thus, we first assign an Ri for every x in the critical layer, then take the median as Ri for the entire layer. To avoid noisiness, the local Ri is computed using the vertical distance over which the local u_x increases from $0.3\times$ its critical value to its critical value. The value 0.3 effectively excludes the self-acceleration induced by the IGW. This can be written

$$
\begin{aligned}
z_{CL,\min}(x,t) &= \operatorname*{argmin}_{\zeta} \left\{ z : u_x(x,\zeta,t) > 0.3\overline{U}_c \right\}, \\
z_{CL,\max}(x,t) &= \operatorname{argmax} \zeta \left\{ z : u_x(x,\zeta,t) < \overline{U}_c \right\}, \\
\mathrm{Ri}(t) &\equiv \operatorname*{med}_{x} \left(\frac{N^2 \left(z_{CL,\max} - z_{CL,\min} \right)^2}{(0.7\overline{U}_c)^2} \right).
\end{aligned}
\tag{28}
$$

To understand the variation in Ri over x, we can also plot using the minimum over x (the maximum is significantly noisier). Both of these are shown in Figure 6. The quick evolution of Ri to its saturated value is reflective of the fact that IGW are *anti-diffusive*. This property is a simple consequence of the IGW dispersion relation Equation 4, which is approximately $\omega k_z \approx N k_x$ such that as an IGW propagates into a shear flow, ω decreases and k_z increases, enhancing dissipation and further driving mean flow acceleration.

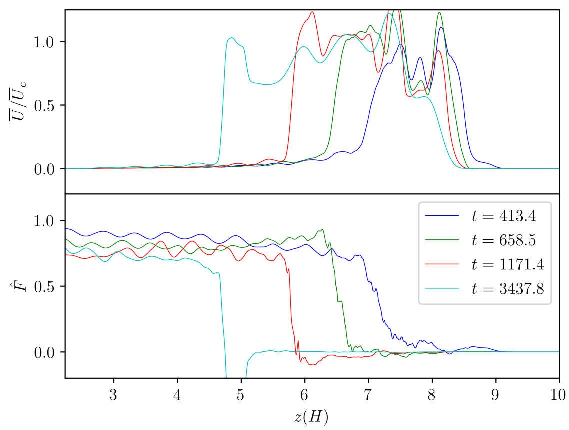

Figure 4. Plot of $\overline{U}(z,t)$ and $\hat{F}(z,t)$ respectively at the same times in Figure 3 over z in our Re = 1024 simulation. $\overline{U}$, $\hat{F}$ follow their definitions in Equation 13 and Equation 22. $\overline{U}$ is given in units of $\overline{U}_c = \frac{\omega}{k_x}$ the critical horizontal flow velocity (see subsection 3.4). The propagation of the critical layer towards lower z and sharp deposition of F at the critical layer are evident.

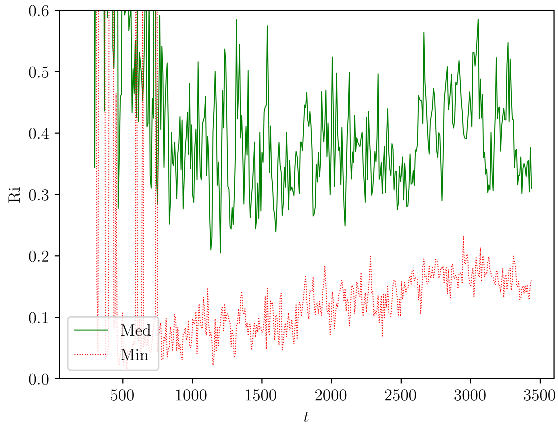

Figure 6. Local Richardson number of the flow at the critical layer over time as defined in Equation 28. The dotted red and solid green lines denote respectively the minimum and median of Ri over x (the maximum greatly exceeds the vertical scale of this plot). These numbers effectively measure the mean and spread in width of the critical layer over x. Note that Ri $\sim \frac{1}{4}$ corresponds to the KHI, so this plot suggests the shear at the critical layer does not steepen past the KHI onset.

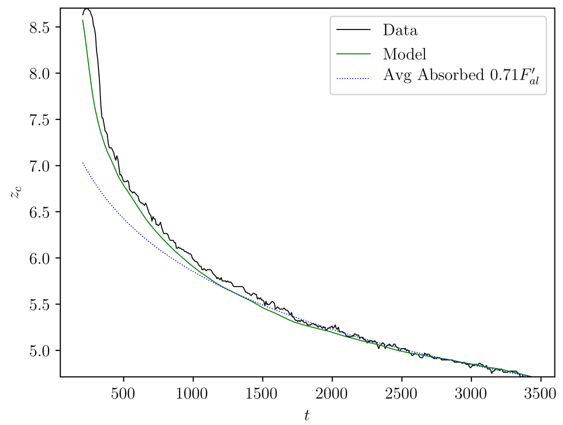

Figure 5. Propagation of the critical layer over time. Shown are (black) $z_c(t)$ from simulation data, (green) predictor of $z_c(t)$ using direct integration of Equation 17 for $\Delta F(t)$ measured from simulation data (described in Equation 27) and (blue) direct substitution of time-averaged $\langle \Delta F(t) \rangle_t$ into Equation 18. Predictors use the end of the simulation as initial conditions and integrate backwards, as z_c is less well-defined at early times. The agreement of the directly-integrated predictor with the data shows Equation 17 is a good description of the evolution of z_c. The the poorer but qualitatively correct agreement of the time-averaged predictor with the data shows both that $\Delta F(t) \neq F'_{al}$ and that $\Delta F(t)$ likely has some very real variation with time.

5.4 Non-absorption at Critical Layer

We identify two manifestations of non-absorptive behavior: (i), the presence of a reflected wave with wave vector $\mathbf{k} = k_x\hat{\mathbf{x}} - k_z\hat{\mathbf{z}}$, and (ii) the amount of horizontal momentum flux F reflected/transmitted by the critical layer. The reflected wave amplitude and reflected flux need not agree exactly if some reflected flux is in higher-order modes, which is indeed the case in our simulations. Both are of physical interest, however: the reflected wave amplitude may be of physical interest in setting up standing modes in a realistic star, while the flux transfer properties is important for accurately tracking angular momentum transfer during synchronization.

To measure the reflected wave amplitude, we use almost the same definition Equation 20 except using $k_z \to -k_z$; call this estimated $\hat{A}_r(t)$ the amplitude of the downwards-propagating reflected wave. To compute $\hat{A}_r(t)$, we furthermore permit an arbitrary phase offset $\phi_r(t)$ at each time t, since the phase of the reflected wave is unknown, unlike that of the incident wave. $\phi_r(t)$ in our simulations behaves in agreement with reflection off a moving boundary at z_c, well approximated by $\left|\frac{\partial \phi_r}{\partial t}\right| \approx 2\left|\frac{\partial (k_z z_c)}{\partial t}\right|$.

Since reflectivity depends sensitively on accurate measurements of $\hat{A}_i, \hat{A}_r$, we remark Equation 20 ensures orthogonality between $k_x\hat{\mathbf{x}} \pm k_z\hat{\mathbf{z}}$ modes. The integral for $\hat{A}_r$ is also performed over $z \in [z_0+3\sigma, z_0+3\sigma+H]$. Since $\hat{A}_i(t), \hat{A}_r(t)$ vary somewhat strongly over time, we perform time averaging over interval approximately $8\pi/\omega$, denoted by angle brackets. We can then define the amplitude reflectivity

$$\mathcal{R}_A(t) \equiv \frac{\left\langle \hat{A}_r \right\rangle(t)}{\left\langle \hat{A}_i \right\rangle(t)}. \tag{29}$$

To measure the reflected horizontal momentum flux, we recall from our linear simulations described in subsection 4.3 that we are able to accurately predict the incident flux from the incident wave amplitude. Thus, we write for incident flux

$$F_i(t) \equiv \langle \rho u_x u_z \rangle_x \hat{A}_i^2(t). \tag{30}$$

But then, since we already have $\Delta F(t), F_>(t)$ jump and transmitted flux across the critical layer at time t respectively, we can immediately write down the reflected flux

$$F_r(t) = F_i(t) + \Delta F(t) - F_>(t). \tag{31}$$

Note that $F_>(t)$ is just the transmitted flux across the critical layer, since there is no other flux above the critical layer. We then define

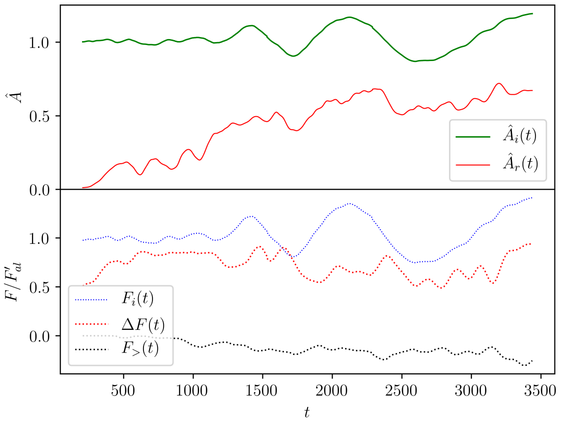

Figure 7. The top panel measures the incident wave amplitude $\hat{A}_i(t)$ (green) and the downwards propagating wave amplitude $\hat{A}_r(t)$ (red) just above the forcing zone, normalized to the analytical estimate Equation 11. $A_d \neq 0$ due to reflection off the critical layer. The bottom panel shows the behavior of three horizontal momentum fluxes over time, in units of the analytical estimate Equation 9: (blue) flux incident on the critical layer, (red) flux absorbed by the critical layer, and (black) flux transmitted through the critical layer.

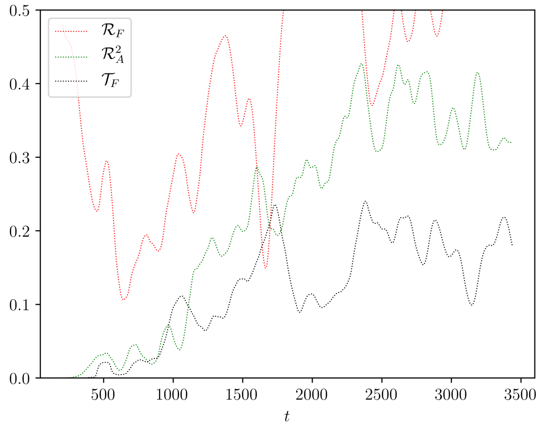

Figure 8. Reflectivity and transmittivity coefficients for flux and amplitude-squared as described by Equation 29 and Equation 32 respectively. The coefficients seem to become comparatively stable past about $t = 1750/N$, indicating that an asymptotic value may have been reached.

flux reflectivity and transmissivity coefficients

$$\mathcal{R}_F(t) \equiv -\frac{\langle F_r \rangle (t)}{\langle F_i \rangle (t)}, \qquad \mathcal{T}_F(t) \equiv -\frac{\langle F_> \rangle (t)}{\langle F_i \rangle (t)}. \tag{32}$$

The measurements of $\hat{A}_i, \hat{A}_r, F_i, \Delta F, F_r, F_>$ are given in Figure 7. The oscillations in $\hat{A}_i, F_i, A_d, F_r$ are significant but the mean values seem to have temporally converged.

Using these measured quantities, we may make plots of $\mathcal{R}_A^2, \mathcal{R}_F, \mathcal{T}_F$, which are provided in Figure 8. A comparison between $\mathcal{R}_A^2$ and $\mathcal{R}_F$ is appropriate as $F \propto A^2$. Visual inspection suggests the three quantities have reached their asymptotic values after $t \gtrsim 1750/N$. An observation may be made that in general $\mathcal{R}_F \geq \mathcal{R}_A^2$; this conforms to the expectation that reflected flux consists of the simple reflected mode and higher order modes as well.

5.5 Convergence

As the primary test of convergence in our previous sections, we consider the convergence of the physically significant parameters of our model. In particular, the convergence of Ri, shown in Figure 6, and of the reflection/transmission coefficient asymptotic values, shown in Figure 8, are of greatest significance.

To estimate convergence, we compute the median value of each of Ri, $\mathcal{R}_A^2, \mathcal{R}_F, \mathcal{T}_F$ over the last 1/4 of simulation times from each simulation, where all simulations had converged to what appeared to be asymptotic values. Error bars are estimated with the 16 and 84 percentiles. We illustrate the convergence of these averages across simulations in Figure 9.

It is apparent that the Richardson number rapidly converges to Ri $\approx$ 0.4 but the reflection/transmission coefficients converge more slowly. This is in disagreement with Equation 15 calculated via the linear analytical theory. This tension is natural: fluid motion within the critical layer is turbulent, so transmission/reflection at the critical layer cannot be captured by any linear theory.

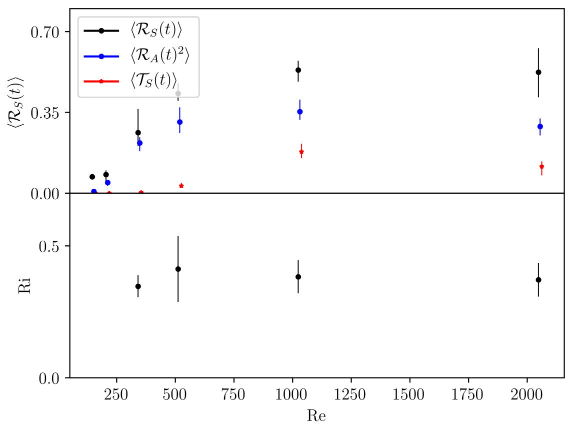

Figure 9. Convergence of median reflection/transmission coefficients and Ri (critical layer width) across runs with varying viscosity, parameterized with Re (Equation 23). Error bars depict 16 and 84 percentile values. Small horizontal displacements are made for data points at identical Re for readability. Note that simulations with larger Re correspond to smaller viscosity and are more physically realistic, and our values seem to converge towards large Re. At the smallest Re value, Ri $\approx$ 50 is too large to fit on the plot.

6 DISCUSSION

In the previous section, we have argued for a continous train of breaking IGWs spontaneously forming a critical layer and strong shear flow. We have parameterized the width of the critical layer as well as horizontal momentum transport near the critical layer. In the subsequent sections, we will discuss the validity of these results and their application to astrophysical systems.

6.1 Physical Sources of Dissipation in WDs

The most significant linear damping in WD g-modes comes from radiative damping (Fuller & Lai 2011). In (Wu 1998) and (Fuller &

Lai 2011), the radiative damping rate is given in terms of $\omega_i = \gamma\omega_r$, where ω_r is the frequency of the g-mode. Typical values for γ range from 10^{-4} to 10^{-11} depending on n of the g-mode.

We will assume this prescription directly transfers to propagating IGW, which results in general agreement with (Burkart et al. 2013)'s estimate of radiative damping rates. Then, making coarse identification $\omega_i \sim \nu k^2 \approx \nu k_z^2$, we find that Re $\sim \frac{1}{\gamma}$. Even at $\gamma = 10^{-4}$ however, the corresponding Re is far too weak to suppress reflection/transmission at the critical layer (e.g. Figure 9).

Another source of dissipation considered in (Burkart et al. 2013) is turbulent conbmtive damping. They find this damping rate to never exceed that of radiative damping, and so it is also too weak to suppress critical layer formation in our problem.

Finally, we consider the impact of magnetic winding. In (Burkart et al. 2013), magnetic winding is used to enforce solid body rotation on the grounds that $t_A \gg t_{gw}$, where

$$t_A = \int_0^R \frac{\sqrt{4\pi\rho}}{B_0}\,\mathrm{d}r \sim 10^2\ \mathrm{yr}\left(\frac{10^3\ \mathrm{G}}{B}\right). \tag{33}$$

the Alfvén wave crossing time (evaluated for a CO WD in Fuller & Lai 2013) measures the magnetic coupling time and t_{gw} measures the gravitational wave inspiral timescale. Before solid body rotation is attained, another relevant timescale is the synchronization timescale t_s. For a tidal torque τ and tidal forcing frequency $\sigma = m\left(\Omega - \Omega_{spin}\right)$, we note that angular momentum transfer is $\frac{\partial M_{sync}}{\partial t}\sigma R^2 = \tau$, where M_{sync} denotes the mass of the WD that has synchronized. Thus, the synchronization timescale is

$$\begin{aligned} t_{sync} &\sim \frac{M_{sync}\sigma R^2}{\tau}, \\ &\sim 2\times 10^5\ \mathrm{yr}\left(\frac{M}{M_\odot}\right)\left(\frac{\sigma}{2\pi/(1\ \mathrm{hr})}\right)\left(\frac{R}{R_\oplus}\right)^2\left(\frac{10^{-14}GM_\odot^2/R_\oplus}{\tau}\right). \end{aligned} \tag{34}$$

A representative τ has been taken from (Burkart et al. 2013). However, since only the outer $\sim 10^{-4}M_\odot$ need be heated for the thermodynamically interesting effects studied in (Fuller & Lai 2013) and (Fuller & Lai 2012b), it seems that magnetic winding cannot absolutely rule out energetic outbursts such as tidal novae resulting from strong shear flows.

6.2 Applicability to Other Astrophysical Systems

[TODO flesh out]

- k_x, k_z: In astrophysical systems, $k_\perp \ll k_r$. While we do not explore different k_x, k_z, ω_1 in this study, with outgoing boundary conditions, there appears at first to be no z length scale other than k_z, so our results would seem to be invariant under rescaling of the z length scale. However, true turbulence is expected to be isotropic at small scales, which may couple k_x, k_z in a way that $k_x \ll k_z$ produces different dynamics than $k_x \lesssim k_z$ as we've studied. This is a numerically difficult regime though, so we defer consideration to future work.
- Validity of plane-parallel approximation? We're all at $\gtrsim 0.9R_{WD}$.
- Solar-type stars (inner conbmtive, outer radiative): different equation of state/stratification but could be qualitatively similar.
- Solar-type stars: In Barker & Ogilvie (2010), inwards-propagating IGW are excited that break via geometric focusing and effect synchronization. They find no reflected wave despite their nonlinear timescales being 10× shorter than their viscous timescale.

It is not immediately clear whether our results here apply when the flux is geometrically focused, but as a hypothesis we assume the convergence in Figure 9 applies under geometric focusing as a zeroth approximation, perhaps as a property of the fluid motion within the geometrically thin critical layer.

Associating $t \sim \nu k^2 \approx \nu k_z^2$ with the visocus timescale and $t_{NL} \sim \mathbf{u}\cdot\nabla \sim \omega$ for the nonlinear timescale, we find their $\lambda = \frac{t_{NL}}{t_L} \sim$ Re our Reynolds number. Our simulations indicate Re $\gtrsim 500$ are required to observe the correct asymptotic behavior in terms of horizontal momentum flux reflection/transmission, so it is possible their lack of reflection is viscosity limited.

6.3 Heating

[TODO elaborate? Need to make plots to check?]

Our equations do not conserve energy, but it seems like more energy can be transmitted in higher modes as viscosity is decreased. Nevertheless, a significant fraction should still be dissipated in the critical layer since a significant energy cascade must happen in the critical layer.

7 ACKNOWLEDGEMENTS

REFERENCES

Andrews D., Mcintyre M. E., 1976, Journal of the Atmospheric Sciences, 33, 2031

Ascher U. M., Ruuth S. J., Spiteri R. J., 1997, Applied Numerical Mathematics, 25, 151

Barker A. J., Ogilvie G. I., 2010, MNRAS, 404, 1849

Booker J. R., Bretherton F. P., 1967, J. Fluid Mech, 27, 513–539

Boyd J. P., 2001, Chebyshev and Fourier spectral methods. Courier Corporation

Brown S., Stewartson K., 1982, Journal of Fluid Mechanics, 115, 217

Burkart J., Quataert E., Arras P., Weinberg N. N., 2013, Monthly Notices of the Royal Astronomical Society, 433, 332

Burns K. J., Vasil G. M., Oishi J. S., Lecoanet D., Brown B., 2016, Dedalus: Flexible framework for spectrally solving differential equations, Astrophysics Source Code Library (ascl:1603.015)

Burns K. J., Vasil G. M., Oishi J. S., Lecoanet D., Brown B. P., 2019, arXiv preprint arXiv:1905.10388

Dosser H. V., Sutherland B. R., 2011a, J. Atmos. Chem., 68, 2844

Dosser H., Sutherland B., 2011b, Physica D: Nonlinear Phenomena, 240, 346

Drazin P., 1977, Proc. R. Soc. Lond. A, 356, 411

Fuller J., Lai D., 2011, MNRAS, 412, 1331

Fuller J., Lai D., 2012a, MNRAS, 421, 426

Fuller J., Lai D., 2012b, ApJL, 756, L17

Fuller J., Lai D., 2013, MNRAS, 430, 274

García-Berro E., Badenes C., Aznar-Siguán G., Lorén-Aguilar P., 2017, MNRAS, 468, 4815

Gilfanov M., Bogdán Á., 2010, Nature, 463, 924

Goldreich P., Nicholson P. D., 1989, ApJ, 342, 1079

Hazel P., 1967, J. Fluid Mech, 30, 775–783

Iben Jr I., Tutukov A. V., 1984, ApJS, 54, 335

Kilic M., Hambly N. C., Bergeron P., Genest-Beaulieu C., Rowell N., 2018, MNRAS, 479, L113

Klostermeyer J., 1991, Geophysical & Astrophysical Fluid Dynamics, 61, 1

Korol V., Rossi E. M., Groot P. J., Nelemans G., Toonen S., Brown A. G. A., 2017, MNRAS, 470, 1894

Lecoanet D., Brown B. P., Zweibel E. G., Burns K. J., Oishi J. S., Vasil G. M., 2014, The Astrophysical Journal, 797, 94

Lecoanet D., Vasil G. M., Fuller J., Cantiello M., Burns K. J., 2016, Monthly Notices of the Royal Astronomical Society, 466, 2181
Lindzen R. S., Holton J. R., 1968, Journal of the Atmospheric Sciences, 25, 1095
Maoz D., Sharon K., Gal-Yam A., 2010, ApJ, 722, 1879
Nelemans G., 2009, Class. Quantum Grav, 26, 094030
Perets H. B., et al., 2010, Nature, 465, 322
Shen K. J., et al., 2018, AJ, 865, 15
Webbink R., 1984, ApJ, 277, 355
Winters K. B., D'Asaro E. A., 1994, J. Fluid Mech, 272, 255–284
Wu Y., 1998, PhD thesis, California Institute of Technology
Zahn J.-P., 1975, A&A, 41, 329

APPENDIX A: FORCING SOLUTION

To solve for the excited wave amplitude in the linear problem, consider the complexified linearized system of equations, then $\frac{\partial}{\partial t} \to -i\omega$, $\frac{\partial}{\partial x} \to ik_x$. Assuming all fields have dependence $u_z(x,z,t) = u_z'(z)e^{ik_x x - i\omega t}$, this gives:

$$\begin{aligned}
\frac{\mathrm{d}u_z'}{\mathrm{d}z} + ik_x u_x' &= 0,\\
-i\omega u_x' + ik_x \varpi' + gHik_x \Upsilon &= 0,\\
-i\omega u_z' + \frac{\mathrm{d}\varpi'}{\mathrm{d}z} + gH\frac{\mathrm{d}\Upsilon}{\mathrm{d}z} - \frac{\varpi'}{H} &= 0,\\
-i\omega\Upsilon - \frac{u_z'}{H} &= Ce^{-\frac{(z-z_0)^2}{2\sigma^2}}.
\end{aligned}$$

We have replaced all partial derivatives with regular derivatives. This can be recast solely in terms of u_z' as

$$\frac{\mathrm{d}^2 u_z'}{\mathrm{d}z^2} - k_x^2 u_z' - \frac{1}{H}\frac{\mathrm{d}u_z'}{\mathrm{d}z} + u_z'\frac{N^2 k_x^2}{\omega^2} = -\frac{gk_x^2}{\omega^2}Ce^{-\frac{(z-z_0)^2}{2\sigma^2}}.$$

The homogeneous solutions are of form $u_{z,\pm}'(z) = e^{\left(\frac{1}{2H} \pm ik_z\right)(z-z_0)}$ where k_z satisfies the dispersion relation Equation 4. We compute the solution to the inhomogeneous ODE by the method of variation of parameters. The Wronskian can be computed

$$W \equiv \det\begin{vmatrix} u_{z,+}' & u_{z,-}' \\ \frac{\mathrm{d}u_{z,+}'}{\mathrm{d}z} & \frac{\mathrm{d}u_{z,-}'}{\mathrm{d}z}\end{vmatrix} = -2ik_z e^{z/H}. \tag{A1}$$

The general solution is then

$$u_z' = -u_{z,+}\int \frac{1}{W}u_{z,-}'\left(-\frac{gk_x^2}{\omega^2}Ce^{-\frac{(z-z_0)^2}{2\sigma^2}}\right)\mathrm{d}z + u_{z,-}\int \frac{1}{W}u_{z,+}'\left(-\frac{gk_x^2}{\omega^2}Ce^{-\frac{(z-z_0)^2}{2\sigma^2}}\right)\mathrm{d}z. \tag{A2}$$

Taking these integrals and applying boundary conditions $u_z'(z\to\infty) = u_{z,+}', u_z'(z\to-\infty) = u_{z,-}'$ gives exact solution

$$u(z) = \frac{C}{2ik_z}\frac{gk_x^2}{\omega^2}e^{\frac{\left(\frac{\sigma^2}{2H}\pm ik_z\sigma^2\right)^2}{2\sigma^2}}\sqrt{2\sigma^2}\frac{\sqrt{\pi}}{2}\left[-u_+(1+\mathrm{erf}(\xi)) + u_-(\mathrm{erf}(\xi)-1)\right] \tag{A3}$$

If we are concerned with only z scales significantly larger than σ, then we may take $\mathrm{erf}(\xi) \approx \Theta(\xi)$. If we further assume $k_z H \gg 1$ and restore the $e^{ik_x x - i\omega t}$ factor, we recover the cited form Equation 11

$$u_z'(x,z,t) = -\frac{C}{2ik_z}\frac{gk_x^2}{\omega^2}e^{-\frac{k_z^2\sigma^2}{2}}\sqrt{2\pi\sigma^2}e^{ik_x x - i\omega t}\times\begin{cases} e^{\left(\frac{1}{2H}+ik_z\right)(z-z_0)+\frac{k_z\sigma^2}{2H}} & z > z_0,\\ e^{\left(\frac{1}{2H}-ik_z\right)(z-z_0)-\frac{k_z\sigma^2}{2H}} & z > z_0.\end{cases} \tag{A4}$$

We use the plane wave approximation in our fitting routines since we generally fit many σ away from z_0, and orthogonality with other modes is essential for a reliable fit.

APPENDIX B: EQUATION IMPLEMENTATIONS

We denote $x \in [0, L_x], z \in [0, L_z]$ the simulation domain and N_x, N_z the number of spectral modes in the respective dimensions.

Numerically, the nonlinear $\frac{\nabla P}{\rho}$ term is problematic: we desire a system where the fluid fields are not divided by one another. We introduce $\varpi = \frac{P}{\rho}$ instead, then mandate $\overline{\rho}, \overline{\varpi}$ background fields satisfy hydrostatic equilibrium $\nabla\overline{\varpi} + \overline{\varpi}\nabla\overline{\rho} + g\hat{\mathbf{z}} = 0$. Taking isothermal stratification, we find $\overline{\varpi} = gH$. We further change variables to $\Upsilon = \ln\rho - \ln\overline{\rho}$ and $\varpi' = \varpi - \overline{\varpi}$ deviations from the background state to obtain a system of equations at most quadratic in fluid fields:

$$\nabla\cdot\mathbf{u}' = 0, \tag{B1a}$$

$$\frac{\partial\Upsilon}{\partial t} + \left(\mathbf{u}'\cdot\nabla\right)\Upsilon - \frac{u_z}{H} = 0, \tag{B1b}$$

$$\frac{\partial u_x}{\partial t} + \left(\mathbf{u}'\cdot\nabla\right)u_x + \frac{\partial\varpi'}{\partial x} + gH\frac{\partial\Upsilon}{\partial x} + \varpi'\frac{\partial\Upsilon}{\partial x} = 0, \tag{B1c}$$

$$\frac{\partial u_z}{\partial t} + \left(\mathbf{u}'\cdot\nabla\right)u_z + \frac{\partial\varpi'}{\partial z} + gH\frac{\partial\Upsilon}{\partial z} + \varpi'\frac{\partial\Upsilon}{\partial z} - \frac{\varpi'}{H} = 0. \tag{B1d}$$

It bears noting that these equations are exactly equivalent to the original Euler equations and hence conserve horizontal momentum.

B1 Artificial Dissipation

The nonlinear terms in the above equations will transfer energy from lower wavenumbers to higher wavenumbers. Since spectral codes have no numerical dissipation, artificial dissipation must be added. To ensure the dissipitive system conserves horizontal momentum exactly, we begin by adding dissipitive terms to the flux-conservative form of the Euler fluid equations Equation 1 (we use stress tensor $\tau_{ij} = P\delta_{ij}$):

$$\nabla \cdot \mathbf{u}' = 0, \tag{B2a}$$

$$\partial_t \rho + \nabla \cdot (\rho \mathbf{u}' - \nu \nabla(\rho - \overline{\rho})) = 0, \tag{B2b}$$

$$\partial_t(\rho \mathbf{u}') + \nabla \cdot (\rho \mathbf{u}'\mathbf{u}' + \mathrm{diag}(\rho \varpi) - \nu \rho \nabla \mathbf{u}) + \rho g \hat{\mathbf{z}} = 0. \tag{B2c}$$

The same ν is used for both the diffusive and viscous term, though this is not required. Since the dissipation is not physical and is purely used for numerical stability, we choose it such that hydrostatic equilibrium is not modified (hence ν acts only on $\rho - \overline{\rho}$).

One last consideration we found necessary was masking out nonlinear terms in the forcing zone with a similar form to Equation 19. In the absence of this mask, a strong mean flow localized to the forcing zone developed. The mask used was

$$\Gamma_{NL}(z) = \frac{1}{2}\left[2 + \tanh\frac{z - (z_0 + 8\sigma)}{\sigma} - \tanh\frac{z - z_B}{\sigma}\right]. \tag{B3}$$

Including the damping layers and forcing terms as described in subsection 4.1, we finally obtain the full system of equations as simulated in Dedalus:

$$\nabla \cdot \mathbf{u}' = 0, \tag{B4a}$$

$$\begin{aligned}\partial_t \Upsilon - \frac{u_z}{H} &= -\Gamma(z)\Upsilon + \frac{F}{\overline{\rho}(z)} e^{-\frac{(z-z_0)^2}{2\sigma^2}} \cos\left(k_x x - \omega t\right), \\ &+ \Gamma_{NL}\left[-\left(\mathbf{u}' \cdot \nabla\right)\Upsilon + \nu\left(\nabla^2\Upsilon + (\nabla\Upsilon)\cdot(\nabla\Upsilon) - \frac{2}{H}\partial_z\Upsilon + \frac{1 - e^{-\Upsilon}}{H^2}\right)\right],\end{aligned} \tag{B4b}$$

$$\begin{aligned}\frac{\partial u_x}{\partial t} + \frac{\partial \varpi'}{\partial x} + gH\frac{\partial \Upsilon}{\partial x} &= -\Gamma(z)u_x + \Gamma_{NL}\left[\nu\nabla^2 u_x - u_x\nu\left(\nabla^2\Upsilon + (\nabla\Upsilon)\cdot(\nabla\Upsilon) - \frac{2}{H}\partial_z\Upsilon + \frac{1 - e^{-\Upsilon}}{H^2}\right)\right. \\ &\left. + 2\nu\left(\left((\nabla\Upsilon)\cdot\nabla\right)u_x - \frac{1}{H}\partial_z u_x\right) - \left(\mathbf{u}'\cdot\nabla\right)u_x - \varpi'\frac{\partial\Upsilon}{\partial x}\right],\end{aligned} \tag{B4c}$$

$$\begin{aligned}\frac{\partial u_z}{\partial t} + \frac{\partial \varpi'}{\partial z} + gH\frac{\partial \Upsilon}{\partial z} - \frac{\varpi'}{H} &= -\Gamma(z)u_z + \Gamma_{NL}\left[\nu\nabla^2 u_z - u_z\nu\left(\nabla^2\Upsilon + (\nabla\Upsilon)\cdot(\nabla\Upsilon) - \frac{2}{H}\partial_z\Upsilon + \frac{1 - e^{-\Upsilon}}{H^2}\right)\right. \\ &\left. + 2\nu\left(\left((\nabla\Upsilon)\cdot\nabla\right)u_z - \frac{1}{H}\partial_z u_z\right) - \left(\mathbf{u}'\cdot\nabla\right)u_z - \varpi'\frac{\partial\Upsilon}{\partial z}\right].\end{aligned} \tag{B4d}$$